OPEN ACCESS



Turbulence and Waves in the Sub-Alfvénic Solar Wind Observed by the Parker Solar Probe during Encounter 10

L.-L. Zhao^{1,2}, G. P. Zank^{1,2}, L. Adhikari², D. Telloni³, M. Stevens⁴, J. C. Kasper^{5,6}, S. D. Bale⁷, and N. E. Raouafi⁸

Center for Space Plasma and Aeronomic Research (CSPAR), The University of Alabama in Huntsville, Huntsville, AL 35805, USA; Iz0009@uah.edu

² Department of Space Science, The University of Alabama in Huntsville, Huntsville, AL 35805, USA

³ INAF Astrophysical Observatory of Torino, Via Osservatorio 20, I-10025 Pino Torinese, Italy

⁴ Smithsonian Astrophysical Observatory, Cambridge, MA 02138, USA

⁵ BWX Technologies, Inc., Washington DC 20002, USA

⁶ Department of Climate and Space Sciences and Engineering, University of Michigan, Ann Arbor, MI 48109, USA

⁷ Physics Department, University of California, Berkeley, CA 94720-7300, USA

⁸ Applied Physics Laboratory, Johns Hopkins University, Laurel, MD 20723, USA

Received 2022 May 16; revised 2022 July 17; accepted 2022 July 22; published 2022 August 4

Abstract

During its 10th orbit around the Sun, the Parker Solar Probe sampled two intervals where the local Alfvén speed exceeded the solar wind speed, lasting more than 10 hours in total. In this paper, we analyze the turbulence and wave properties during these periods. The turbulence is observed to be Alfvénic and unbalanced, dominated by outward-propagating modes. The power spectrum of the outward-propagating Elsässer z^+ mode steepens at high frequencies while that of the inward-propagating z^- mode flattens. The observed Elsässer spectra can be explained by the nearly incompressible (NI) MHD turbulence model with both 2D and Alfvénic components. The modeling results show that the z^+ spectra are dominated by the NI/slab component, and the 2D component mainly affects the z^- spectra at low frequencies. An MHD wave decomposition based on an isothermal closure suggests that outward-propagating Alfvén and fast magnetosonic wave modes are prevalent in the two sub-Alfvénic intervals, while the slow magnetosonic modes dominate the super-Alfvénic interval in between. The slow modes occur where the wavevector is nearly perpendicular to the local mean magnetic field, corresponding to nonpropagating pressure-balanced structures. The alternating forward and backward slow modes may also be features of magnetic reconnection in the near-Sun heliospheric current sheet.

Unified Astronomy Thesaurus concepts: Solar coronal waves (1995); Interplanetary turbulence (830); Solar wind (1534)

1. Introduction

One of the main science objectives of the Parker Solar Probe (PSP) is to understand the heating and acceleration of the solar wind near the Sun (Fox et al. 2016). Turbulence is thought to play an important role in this problem. The dissipation of lowfrequency turbulence close to the Sun provides a possible heating mechanism for the solar corona and solar wind (e.g., Matthaeus et al. 1999; Zank et al. 2018, 2021). As PSP travels closer to the Sun, it is revealing the changing properties of solar wind turbulence. For example, solar wind turbulence is observed to be highly Alfvénic in the near-Sun region observed by PSP, which is indicated by highly correlated velocity and magnetic field fluctuations and increasing cross-helicity (Chen et al. 2020). The relative turbulent fluctuation amplitude increases as the radial distance decreases (e.g., Adhikari et al. 2020). The power ratio of the two-dimensional (2D) fluctuations appears to be smaller than that observed at 1 au (Bandyopadhyay & McComas 2021; Zhao et al. 2022a), although this conclusion is tempered by assumptions related to the form of the underlying spectra. The magnetic compressibility, i.e., the ratio between the magnetic field magnitude fluctuations and the total magnetic trace fluctuations, increases

Original content from this work may be used under the terms of the Creative Commons Attribution 4.0 licence. Any further distribution of this work must maintain attribution to the author(s) and the title of the work, journal citation and DOI.

with radial distance (Bale et al. 2019; Chen et al. 2020; Telloni et al. 2021). The turbulence energy cascade rate is higher near the Sun than at 1 au (e.g., Bandyopadhyay et al. 2020; Andrés et al. 2021).

After entering the sub-Alfvénic flow in 2021 April 28 for the first time (Kasper et al. 2021), PSP sampled prolonged periods of sub-Alfvénic intervals during its subsequent orbits. The sub-Alfvénic region is where the primary solar wind acceleration occurs. It is characterized by a local Alfvén speed that exceeds the solar wind speed, which indicates the domination of magnetic energy over kinetic energy. The Alfvén critical surface where the solar wind speed equals the Alfvén speed is expected to be located around 10-20 solar radii from the Sun. The transition from the super- to the sub-Alfvénic regime is important. Outside the Alfvén critical surface, both inward- and outward-propagating Alfvén waves are advected outward by the solar wind flow. The inward-propagating Alfvén waves originating within the Alfvén critical surface cannot escape into the super-Alfvénic solar wind. Therefore, turbulence in the two regions may exhibit different properties. The first sub-Alfvénic flow observed by PSP is at about 20 solar radii and lasts for \sim 5 hours with a median Alfvén Mach number of 0.79. The turbulence properties within this sub-Alfvénic flow have been studied from many aspects (Kasper et al. 2021; Zhao et al. 2022b; Bandyopadhyay et al. 2022; Zank et al. 2022). Specifically from the limited observations of the sub-Alfvénic solar wind during the eighth and ninth orbits of PSP, it is found that turbulence within the sub-Alfvénic region has weaker magnetic compressibility and intermittency (Bandyopadhyay et al. 2022). The power spectral density analysis of the Elsässer variables shows a flattening of the inward-propagating modes at high frequencies (Zhao et al. 2022a; Zank et al. 2022), which may be explained by the nearly incompressible (NI) turbulence model (Zank et al. 2017, 2020), although the possible influence of noise has not been quantified.

More recently, PSP sampled two more sub-Alfvénic intervals during its 10th orbit around the Sun. These intervals lasted longer (~8 hr), with an Alfvén Mach number as small as ~0.2. They provide new opportunities to investigate this novel physical regime and validate previous observations. In this paper, we present an analysis of the turbulence power spectra, including the spectra of magnetic fluctuations, velocity fluctuations, and the Elsässer fields in the two sub-Alfvénic flows observed during the 10th orbit of PSP. We also analyze MHD-scale wave properties based on an MHD mode decomposition assuming an isothermal closure. The observational analysis presented here is helpful for furthering our understanding of turbulence in the sub-Alfvénic solar wind.

2. Data Overview

Figure 1 shows an overview of the plasma environment during the crossing of the two sub-Alfvénic solar wind intervals by PSP during encounter 10 from 2021 November 21, 15:00 UT, to November 22, 18:00 UT. We use magnetic field data from the PSP/FIELDS Fluxgate Magnetometers (MAGs) measurements (Bale et al. 2016), electron density n_e data from the peak in the quasi-thermal noise (QTN) spectrum measured by the PSP/FIELDS Radio Frequency Spectrometer (RFS) (Moncuquet et al. 2020), ion partial moments data from the PSP/Solar Probe ANalyzer-Ions (SPAN-I) instrument (Kasper et al. 2016), and the thermal electron pitch angle distribution (PAD) from Solar Probe ANalyzer-Electron (SPAN-E) instrument (Whittlesey et al. 2020). The proton density n_p is roughly consistent with the electron density n_e during the period of interest, suggesting that the proton distribution measured by SPAN-I is largely reliable. In the following analysis, we use the QTN density n_e as a proxy for the plasma density unless n_e is unavailable for 6 consecutive minutes, in which case the SPAN-I density n_p is used. The two sub-Alfvénic intervals, indicated by green and pink shaded areas, are characterized by a low Alfvén Mach number, i.e., $M_A < 1$, and a lower solar wind kinetic energy relative to magnetic energy. Here, M_A is the ratio between the plasma radial speed V_R and the Alfvén speed $V_A = |B|/\sqrt{4\pi n_p m_p}$, with |B| the magnetic field magnitude and n_p the plasma number density. We used the pointwise density when calculating V_A to further calculate M_A over time shown in Figure 1. Compared with the surrounding super-Alfvénic winds, the field magnitude |B| in the two sub-Alfvénic flows increases slightly, i.e., closer to the expected $1/r^2$ Parker spiral scaling, with r the radial distance (purple dashed line in the top panel). The sub-Alfvénic intervals are also characterized by reduced flow speed and density, and fewer switchbacks (Kasper et al. 2019). In addition, the PAD of 540 eV electrons shows some weakly unidirectional behavior in the first sub-Alfvénic flow compared to the preceding super-Alfvénic wind, i.e., the anti-field-aligned (PA $\sim 180^{\circ}$) Strahl electron flux is significantly reduced. These features may be interpreted as being consistent with the generation of switchbacks by magnetic-reconnection-related mechanisms (Fisk &

Kasper 2020; Zank et al. 2020; Bale et al. 2021; Drake et al. 2021). The observed sub-Alfvénic intervals may be reasonably far from boundaries between flows and/or distinct magnetized regions and may therefore correspond to less magnetic reconnection eroding the magnetic field and generating fewer switchbacks. In contrast, the surrounding super-Alfvénic intervals may have been processed by coronal magnetic reconnection more and thus have lower magnetic field strength, faster wind speed, more heated electrons, and more switchbacks. Specifically, in the interchange-reconnection picture proposed by Zank et al. (2020), the slow solar wind originates from an interchange-reconnection event between a large loop and an open field region (Zank et al. 2021), and switchbacks should occur primarily on the borders of slow and fast winds. If PSP happens to measure the middle of a slow wind, switchbacks cannot be detected.

During the super-Alfvénic interval between two sub-Alfvénic winds (\sim 01:00–02:40 UT), as the magnetic field magnitude |B| drops to near zero, there is a corresponding sharp increase in M_A (>10). The decrease of |B| is also associated with an abrupt change in the radial magnetic field B_R . The deep plunge in |B| is likely related to the heliospheric current sheet (HCS) crossing. In fact, there is another similar but more moderate drop of |B| near 12:00 UT on November 22. However, because the radial magnetic field B_R does not change direction during both periods and there is no significant and long-lasting reversal in the direction of the electron Strahl propagation, a complete HCS crossing was likely not observed, but these may instead be associated with partial HCS crossings (e.g., Phan et al. 2021). Although close to the partial HCS crossing, the two sub-Alfvénic regions reported here are not expected to be significantly affected by the HCS. As shown in the top panel, the field magnitude in both sub-Alfvénic intervals follows the predicted $1/r^2$ scaling. The region that is significantly affected by HCS should have a much lower field amplitude. Near the boundary, it could be affected by the HCS somehow, but the specific effects need to be further studied. In addition, the first sub-Alfvénic interval lasts more than 3 hr, and the second sub-Alfvénic interval is more than 7 hr. The minimum Alfvén Mach number in both intervals is less than 0.5. This persistently low M_A and rigorous $1/r^2$ field scaling suggest that a robust sub-Alfvénic corona wind is observed (Badman et al. 2020; Kasper et al. 2021).

In the bottom three panels of Figure 1, we show the spectrogram of the normalized reduced magnetic helicity σ_m , normalized cross-helicity σ_c , and normalized residual energy σ_r from a wavelet analysis (Zhao 2020, 2021c, 2021b). The wavelet scale ranges from 8 to 256 minutes and contains the turbulent inertial range and energycontaining range. In plotting these spectrograms, we use a 2 hr moving average to calculate the background mean magnetic and velocity fields, which are then subtracted respectively to obtain the fluctuating magnetic field $\delta \mathbf{B}$ and velocity $\delta \mathbf{v}$. The normalized turbulence quantities $\sigma_m = 2 \operatorname{Im}(\delta \tilde{\boldsymbol{B}}_T^* \delta \tilde{\boldsymbol{B}}_N) / \operatorname{Tr}(\boldsymbol{B}),$ $\sigma_c = 2\langle \delta \mathbf{v} \cdot \delta \mathbf{b} \rangle / (\langle \delta \mathbf{v}^2 \rangle + \langle \delta \mathbf{b}^2 \rangle),$ $\sigma_r = (\langle \delta v^2 \rangle - \langle \delta b^2 \rangle) / (\langle \delta v^2 \rangle + \langle \delta b^2 \rangle)$ are then calculated. Here, the tilde denotes wavelet-transformed quantities, Tr(B) the magnetic trace spectrum, and $\delta \mathbf{b} = \delta \mathbf{B} / \sqrt{4\pi n_p m_p}$ is the magnetic fluctuation in Alfvén units. The density here is also calculated using the 2 hr moving average when generating the spectrograms of σ_c and σ_r . As shown in the figure, the predominantly positive σ_c suggests that outwardly propagating

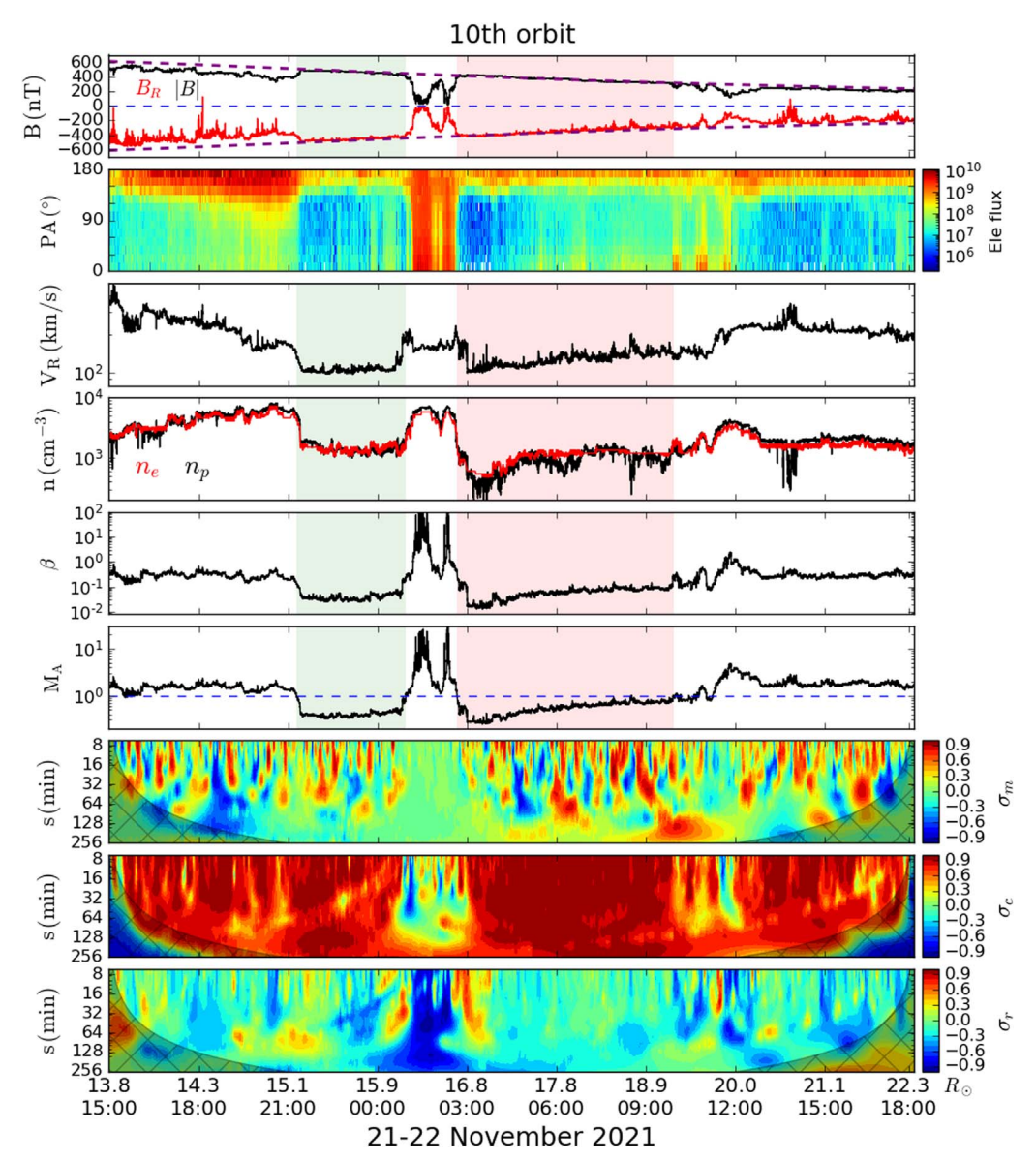


Figure 1. Solar wind parameters observed by PSP during E10. Panels from top to bottom show the magnetic field radial component B_R (red line), magnitude |B| (black line), and the $1/r^2$ field scaling (purple dashed line) predicted by the Parker spiral model, PAD of 526 eV superthermal electrons from SPAN-E, solar wind proton radial speed V_R , proton density n_p from SPAN-I (black line) and electron density n_e from the QTN spectrum (red line), proton plasma beta β , and radial Alfvén Mach number M_A ; and the spectrogram of the normalized reduced magnetic helicity σ_m , normalized cross-helicity σ_c , and normalized residual energy σ_r . The shaded cross areas in the bottom three panels are determined by the cone of influence (COI) during the wavelet transform. Scales larger than the COI are subject to edge effects and are not reliable. The two sub-Alfvénic solar wind intervals are indicated by green and pink shaded areas, respectively.

Alfvén waves dominate during the period of interest, which is also illustrated by the close-to-zero σ_r values. There are some patches of positive and negative magnetic helicity σ_m . However, during the super-Alfvénic regions embedded in possible HCS crossings (i.e., \sim 01:00–02:40 UT and 12:00 UT), σ_m is close to zero, and no magnetic helical structure is identified at the studied scale. However, we note that the two regions are also associated with a close-to-zero cross-helicity σ_c and negative residual energy σ_r . These features suggest that the turbulence here is not dominated by counterpropagating Alfvén waves, which would possess nearly zero residual energy. We will show later that compressible waves or structures are dominant in the interval.

Figure 2 shows the time evolution of various turbulence quantities during the crossing of the two sub-Alfvénic intervals in encounter 10 (E10). Each quantity is calculated over 162

nonoverlapping 10 minute intervals. The top panel shows the amplitude of the forward- and backward-propagating Elsässer variables $z^{\pm} = \delta v \pm \delta b$, and the amplitudes of δv and δb are shown in the second panel. Here the embedded plasma density in δb is the average of each 10 minute interval. Overall, it is consistent with the spectrograms shown in Figure 1. For example, (i) the outward-propagating z^+ mode dominates the entire interval, except for the periods associated with the possible partial HCS crossings; (ii) the magnetic fluctuation amplitude $|\delta b|$ is slightly larger than the kinetic fluctuation amplitude $|\delta v|$, resulting in a negative and close-to-zero σ_r ; (iii) near the possible partial HCS crossings, the turbulence appears to be balanced ($\sigma_c \sim 0$) and dominated by magnetic fluctuations $(\sigma_r < 0)$. In the fifth panel, we show the angle between the mean magnetic field and mean velocity field θ_{VB}^{sc} , which is usually used as a diagnosis of the wavevector anisotropy based

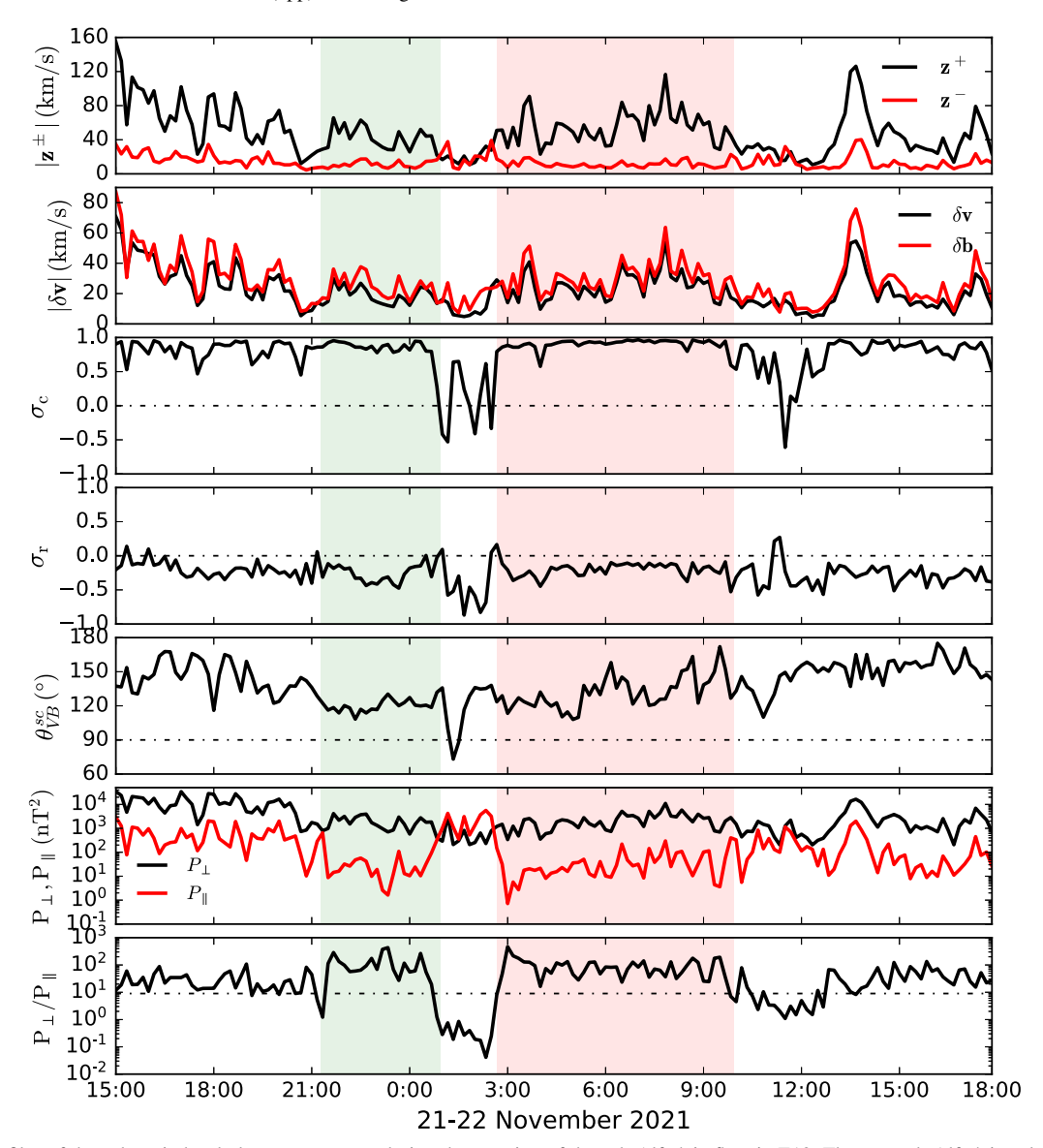


Figure 2. Time profiles of the solar wind turbulence parameters during the crossing of the sub-Alfvénic flow in E10. The two sub-Alfvénic solar wind intervals are indicated by the shaded areas as Figure 1. From top to bottom, the panels show the amplitude of the Elsässer variables z^{\pm} , amplitude of the velocity fluctuations δv and magnetic field fluctuations in Alfvén units δb , normalized cross-helicity σ_c , normalized residual energy σ_r , the angle between the mean magnetic field and mean velocity field in the spacecraft frame $\theta_{\rm VCB}^{\rm sc}$, the transverse P_{\perp} and longitudinal P_{\parallel} magnetic fluctuation power, and the magnetic fluctuation power anisotropy P_{\perp}/P_{\parallel} .

 ${\bf Table~1} \\ {\bf Fluctuation~Amplitudes~in~the~Two~Sub-Alfv\'enic~Flows~Observed~by~PSP~in~E10} \\$

Start Time (UT)	End Time (UT)	$M_A^{ m min}$	$\langle M_A angle$	$\langle z^+ \rangle$ (km s ⁻¹)	$\langle z^- \rangle$ (km s ⁻¹)	$\langle \delta v \rangle$ (km s ⁻¹)	$\langle \delta b \rangle$ (km s ⁻¹)	$\langle \sigma_c \rangle$	$\langle \sigma_r \rangle$	$\langle heta_{\mathrm{VB}}^{\mathrm{sc}} angle \ (^{\circ})$
2021-11-21 21:17	2021-11-22 00:56	0.32	0.42	42	11	19	24	0.8	-0.3	120
2021-11-22 02:40	2021-11-22 09:55	0.24	0.55	55	11	25	31	0.9	-0.2	134

Notes. M_A^{\min} denotes the minimum radial Alfvén Mach number during the interval. The angle brackets $\langle ... \rangle$ represent averaging over the time interval.

on Taylor's hypothesis. Because of the large azimuthal spacecraft velocity (e.g., approximately 138 km s $^{-1}$ in the first sub-Alfvénic interval and 121 km s $^{-1}$ in the second interval), the angle $\theta_{\rm VB}^{\rm sc}$ deviates from the quasi-parallel scenario for both sub-Alfvénic intervals although the magnetic field remains approximately radial. In summary, the averaged values of these quantities over each sub-Alfvénic interval are listed in Table 1.

In the last two panels of Figure 2, we show the magnetic transverse (incompressible) fluctuation power P_{\perp} , the

longitudinal (compressible) fluctuation power P_{\parallel} , and the ratio P_{\perp}/P_{\parallel} . We project the in situ measured magnetic field data with a resolution of \sim 0.22 s to the mean-field-aligned coordinate system (Zhao et al. 2022a). The fluctuation power P_{\parallel} and P_{\perp} at each 10 minute interval are calculated from the variance of δB_{\parallel} and δB_{\perp} , respectively. The black horizontal dashed–dotted line in the last panel denotes the average magnetic power anisotropy $P_{\perp}/P_{\parallel}=9$ found by Belcher & Davis (1971). As shown in the figure, the two sub-Alfvénic

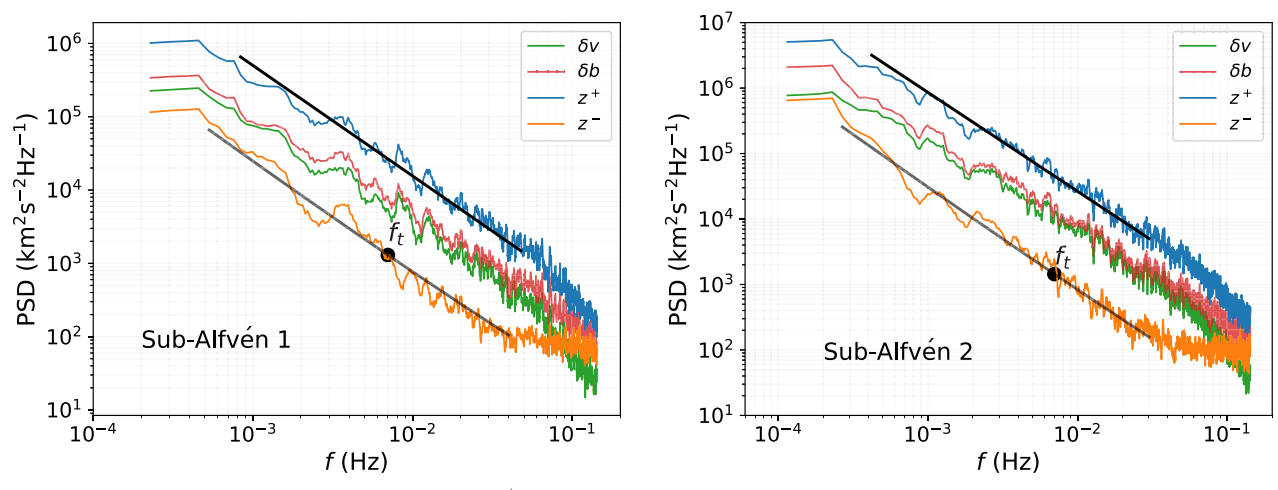


Figure 3. Power spectral density (PSD) of the Elsässer variables z^{\pm} , velocity fluctuations δv , and magnetic fluctuations in Alfvén units δb . The left and right panels correspond to the first and second sub-Alfvénic interval observed in E10, respectively. The black lines in each panel represent the theoretical spectra predicted by the NI MHD turbulence model, and f_t denotes the transition frequency at which the z^- spectrum flattens in the inertial range.

intervals are characterized by a large proportion of incompressible fluctuation power such that P_\perp/P_\parallel is almost 10 times larger than the surrounding super-Alfvénic flow, which has values slightly above 9. However, during the super-Alfvénic interval in between, the compressible fluctuation power P_\parallel increases significantly, and P_\perp/P_\parallel drops to about 0.1. The power anisotropy P_\perp/P_\parallel also decreases slightly at around 12:00 UT. These two drops of P_\perp/P_\parallel are near the possible partial HCS crossings shown in Figure 1 and are mainly related to an increase in compressible fluctuation power P_\parallel , which implies the presence of compressible waves or structures in these regions.

Figure 3 shows the power spectra of the Elsässer variables z^{\pm} , velocity fluctuations δv , and magnetic fluctuations in Alfvén units δb in the two sub-Alfvénic intervals. All the spectra are computed by applying a Fourier transform to each component of the corresponding fluctuations. The total power spectrum shown in the figure is then calculated by the trace of the spectral matrix. We note that the z^+ , δv , and δb spectra exhibit similar behavior in the intermediate-frequency range, with the spectra gradually steepening at higher frequencies. Overall, the z^+ , δv , and δb spectra in the intermediatefrequency range (e.g., ≤0.03 Hz) appear to be consistent with the -1.5 Iroshnikov-Kriachnan (IK) spectrum, as was also reported in Zank et al. (2022) and Zhao et al. (2022b). However, the z^- spectra exhibit very different behavior. For example, the z^- spectrum appears slightly steeper at lower frequencies than the other three quantities and gradually flattens at higher frequencies, exhibiting a concave shape in the inertial range. A natural question is whether the flattening of the z^- spectra at around 10^{-2} Hz is physical or due to noise. Because neither the velocity δv nor magnetic δb power spectra flatten at high frequencies, the noise level is not clear. However, the amplitude of the velocity spectrum is lower than the z^- spectrum at the highest frequencies, which suggests that the noise level is likely to be even lower. Typically, the spectral noise in the Elsässer variables z^{\pm} is dominated by the velocity measurements, so we may cautiously assume that the flattening of the z^- spectra is not due to noise.

The flattening of the z^- spectrum has also been reported in the previous sub-Alfvénic interval observed by PSP (Zhao et al. 2022a; Zank et al. 2022), suggesting physical processes may

be present. A theoretical explanation can be provided by the nearly incompressible (NI) turbulence model, which includes a 2D component and an NI/slab component (Zank et al. 2017). In the NI turbulence model, the flattening of the z^- spectrum is possible for some parameters (see Zank et al. 2020, for details). In our previous study of the sub-Alfvénic solar wind (Zank et al. 2022), we fit the observed Elsässer spectra with the NI/ slab component only because of the approximately aligned solar wind flow and mean magnetic field (i.e., $\theta_{VB}^{sc} \sim 0$), which implies that the observed turbulence is predominantly NI/slab component. In the NI/slab turbulence, as the z^- mode propagates toward the Sun at the Alfvén speed V_A (in the opposite direction to the z^+ mode), the corresponding length scales of the z^- and z^+ modes can be vastly different at the same observed frequency. Based on the assumption that the observed z^{\pm} modes are characteristics of forward and backward Alfvén waves, the wavenumber of z^{\pm} at the same frequency differ by a Doppler-shift factor $k_+/k_- = (|U_0\cos\Psi + V_{A0}|)/(|U_0\cos\Psi - V_{A0}|),$ where $\Psi = \theta_{\rm VB}^{\rm sc}$ is the angle between the mean magnetic field $\textbf{\textit{B}}_0$ and mean solar wind speed U_0 in the spacecraft frame, and V_{A0} is the mean Alfvén speed during the interval, which we calculated using the averaged density and mean-field strength $|\mathbf{B}_0|$ within each sub-Alfvénic interval (see Zhao et al. 2022b; Zank et al. 2022, for details). This effect was also considered by Goldstein et al. (1986) as a possible explanation for the observed imbalance in solar wind turbulence.

However, during the two sub-Alfvénic intervals observed in E10, the angle $\theta_{\rm NE}^{\rm sc}$ is highly oblique as shown in Table 1, so both 2D and NI/slab components need to be included to fit the observed Elsässer spectra. For the 2D component, we assume that it contains equal power in the z^+ and z^- modes (as there is no physical reason to assume otherwise), and we assume that they each follow a simple power law with a-5/3 index. Because the 2D component is nonpropagating, the z^+ and z^- modes from the 2D component are not Doppler shifted (Zank et al. 2022). In contrast, as discussed above, the z^+ modes in the NI/slab component are Doppler shifted because they are Alfvénic. Therefore, in the NI MHD turbulence model we employed here, the large difference between the z^+ and z^- power is mainly caused by the NI/slab component, and the 2D component can contribute a fraction of the observed z^-

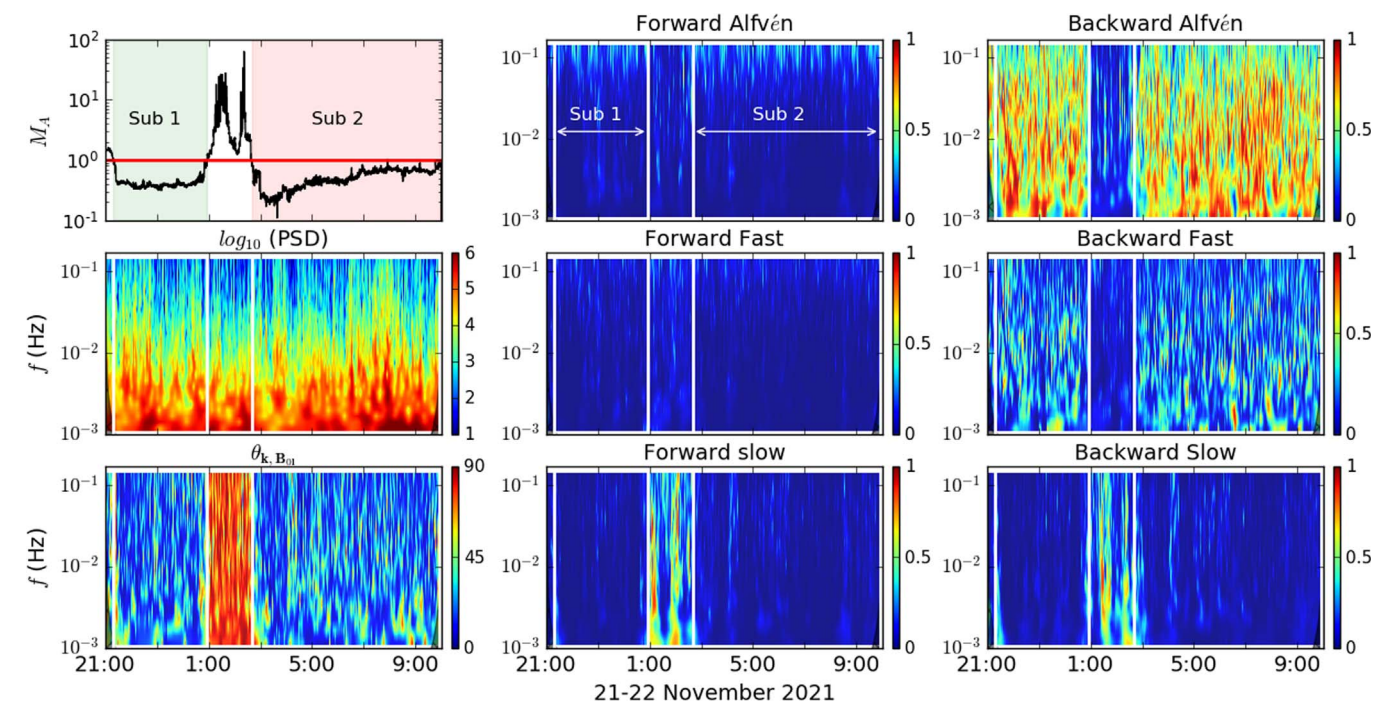


Figure 4. MHD wave mode decomposition from 21:00 on November 21 to 10:00 on November 22. The left panels from top to bottom show the Alfvén Mach number M_A , the wavelet trace PSD of the magnetic field fluctuations, and the angle between wavevector k and the local mean magnetic field $\theta_{k,B_{0l}}$. The other six panels show the relative fraction of the spectral energy density in each MHD wave mode.

spectrum, but its contribution to the observed z^+ spectrum is negligible relative to the NI/slab component.

Based on the above discussion, we construct the black lines in Figure 3 as theoretical predictions of the Elsässer spectra through the NI MHD turbulence model (including both 2D and NI/slab components). The NI/slab component follows the same spectral shape as in Zank et al. (2022). The additional 2D component we considered here has equal power in z^+ and z^- and follows a -5/3 scaling. To summarize, the specific form of the Elsässer spectra based on NI MHD turbulence model used in this paper is given by (see Zank et al. 2020, 2022, for details)

$$G^{+}(k_{+}) \simeq C^{*+}k_{+}^{-3/2} + C^{\infty}k_{+}^{-5/3},$$
 (1)

$$G^{-}(k_{-}) \simeq C^{*-}k_{-}^{-3/2} \left(1 + \left(\frac{k_{-}}{k_{t}}\right)^{\frac{1}{2}}\right)^{\frac{1}{2}} + C^{\infty}k_{-}^{-5/3}, \tag{2}$$

where $k_{\pm}=2\pi f/(|U_0\cos\Psi\mp V_A|)$ are the wavenumber of z^{\pm} . k_t (f_t) is the transition wavenumber (frequency) representing the transition from the nonlinear interaction-dominated to the Alfvénic interaction-dominated regions of spectral space. $C^*\pm$ are the NI/slab power in the forward (z^+) and backward (z^-) propagating modes. C^{∞} is the power of the z^+ and z^- 2D fluctuations (assumed to be equal). To fit the observed Elsässer spectra, we obtain $C_1^{\infty}=4\times10^{-4}~{\rm km^{1/3}s^{-1}},$ $C_2^{\infty}=1\times10^{-3}~{\rm km^{1/3}s^{-1}},$ $C_1^{*+}=4\times10^{-2}~{\rm km^{1/2}s^{-1}},$ $C_2^{*+}=7\times10^{-2}~{\rm km^{1/2}s^{-1}},$ $C_{1,2}^{*-}=2\times10^{-3}~{\rm km^{1/2}s^{-1}},$ and $f_t=7\times10^{-3}~{\rm Hz}.$ Here, the subscript "1" denotes the first sub-Alfvénic interval (left panel) and "2" the second sub-Alfvénic interval (right panel). We find that the z^+ spectrum is dominated by the NI/slab component, which follows a power law of $f^{-3/2}$ in the inertial range. The 2D component we

included simply follows $f^{-5/3}$ for both z^+ and z^- modes, and it mainly affects the z^- power at low frequencies (e.g., $\leq f_t$). The slightly "concave" spectrum of the z^- mode is successfully reproduced by the NI model. For example, it transitions from approximately $f^{-1.55}$ to $f^{-1.48}$ for the first sub-Alfvénic flow, and from $f^{-1.58}$ to $f^{-1.51}$ for the second sub-Alfvénic interval. As shown in the figure, the model is reasonably consistent with the observed Elsässer spectra within an intermediate-frequency range. Note that the flattening of the z^- spectrum at the highest frequencies (near 0.1 Hz) is not explained by the NI turbulence model

In Figure 4, we present an MHD wave decomposition for the two sub-Alfvénic intervals and the intervening interval. The top-left panel shows the Alfvén Mach number M_A as a reference. The left-middle panel plots the trace spectrum of the magnetic fluctuations in the frequency range of 10^{-3} Hz to 10^{-1} Hz. The left-bottom panel shows θ_{k,B_0} the angle between wavevector k and the scale-dependent local mean magnetic field B_{0l} (Horbury et al. 2008). We use the singular value decomposition (SVD) method to estimate the scale and timedependent wavevector direction based on the solenoidal condition $\mathbf{k} \cdot \delta \mathbf{B} = 0$ (Santolík et al. 2003). It should be noted that the wavevector direction estimated from the SVD method is different from the local solar wind velocity direction based on Taylor's hypothesis. The angle $\theta_{k,B_{0l}}$ is mostly quasi-parallel in the sub-Alfvénic intervals and is close to perpendicular in the super-Alfvénic interval in between. The middle and right panels in Figure 4 are the results of an MHD wave mode decomposition. Following the method of Glassmeier et al. (1995), an arbitrary set of fluctuating magnetic field, velocity, and plasma density components are decomposed into fast and slow magnetosonic modes and Alfvén modes, each consisting of forward- and backward-propagating (with respect to the mean magnetic field) components. The MHD

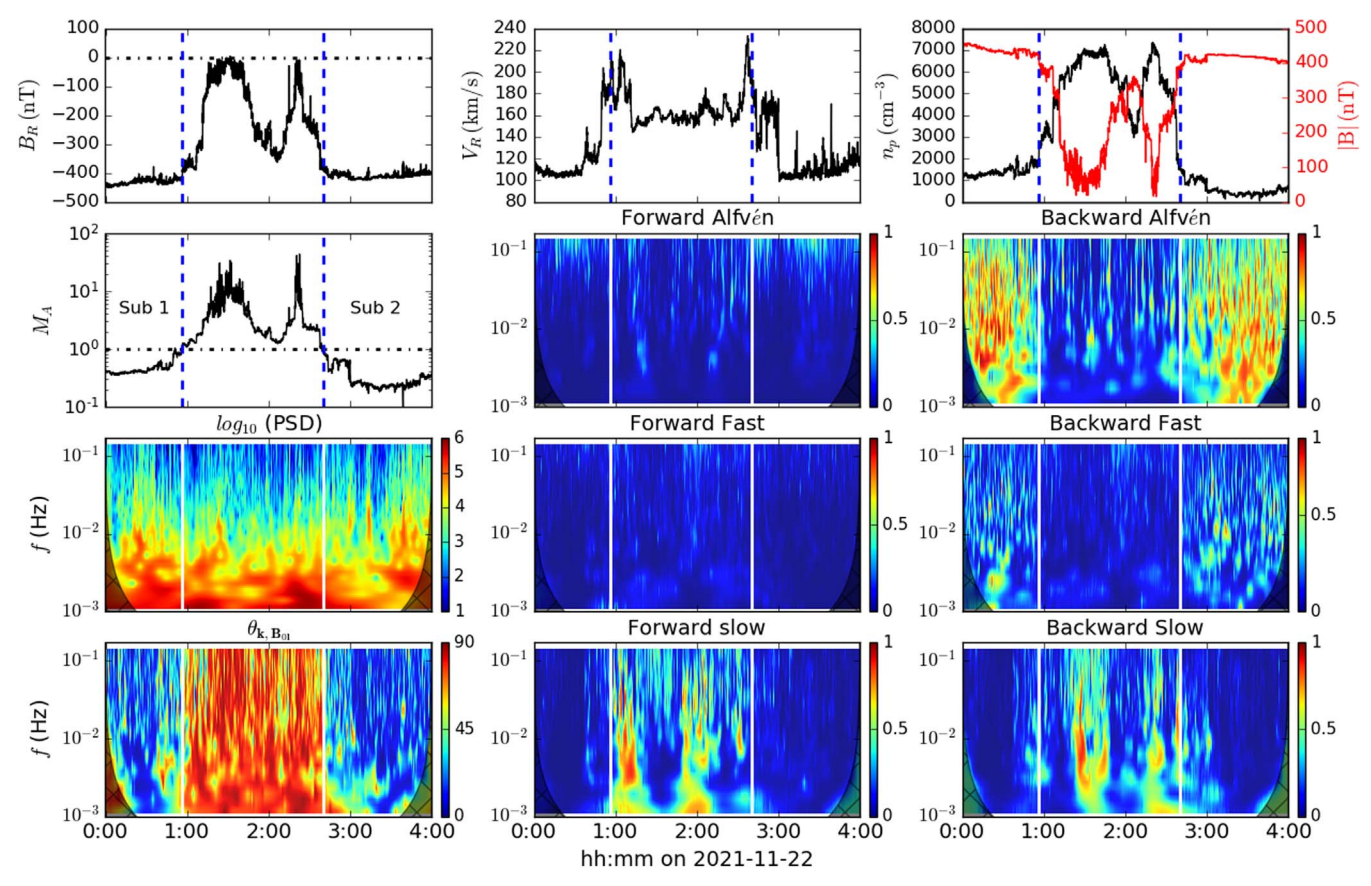


Figure 5. A magnified view of the super-Alfvénic interval between the two sub-Alfvénic flows. The top three panels show the radial magnetic field B_R , radial proton speed V_R , density n_P , and magnetic field magnitude |B|. The other panels have the same format as Figure 4.

decomposition can be done with the standard Fourier spectral analysis as well as the wavelet analysis.

The method proposed in Glassmeier et al. (1995) is based on the linearized MHD equations, the eigenvector system of which provides a complete orthogonal basis for the decomposition of six fluctuating quantities (density, three components of velocity, and two solenoidal components of magnetic field) into the six linear modes. We note that Glassmeier et al. (1995) implicitly assume an isothermal equation of state, which means that the thermal pressure P relates to the mass density ρ via $P = \rho c_s^2$, where c_s is the isothermal sound speed that is a constant. This assumption is also made in subsequent works (e.g., Chaston et al. 2020; Zhu et al. 2020; Zhao et al. 2021a), including the present one. As a result of the isothermal assumption, the nonpropagating entropy mode is eliminated. In reality, the temperature is not a constant and the isothermal assumption cannot be valid. However, the identification of an Alfvén mode requires only the velocity and magnetic field in principle and thus is unaffected by the isothermal closure. For fast and slow magnetosonic modes, a constant isothermal sound speed can have some effects on the decomposition. Specifically, part of the density fluctuations will not be proportional to the pressure fluctuations, and they are caused by the zero-frequency entropy mode. However, as long as the nonpropagating zero-frequency entropy mode is not dominant, we do not expect it to affect the results significantly for the purpose of quantifying the importance of the Alfvén and magnetosonic modes. The inclusion of the entropy mode is deferred to a future study.

Figure 4 suggests that the two sub-Alfvénic intervals are dominated by backward-propagating Alfvén modes, with a minority backward-propagating fast mode. Since $B_R < 0$ during the period, backward propagation represents outward propagating from the Sun. This finding is consistent with our previous analysis of magnetic-field-aligned solar wind intervals observed by PSP (Zhao et al. 2021a). Interestingly, the super-Alfvénic period in between shows a clear domination of alternating forward and backward slow magnetosonic modes with $\theta_{k,B_{0l}} \sim 90^{\circ}$. It is known from the linear wave dispersion relations that in the perpendicular wavevector limit, i.e., $\theta_{k,B_0} \sim 90^{\circ}$, both Alfvén and slow modes have zero frequency and do not propagate. The Alfvén mode reduces to a vortical or magnetic-island-like structure while the slow mode reduces to a pressure-balanced structure. Therefore, the detection of slow modes here indicates the presence of nonpropagating pressurebalanced structures, which may originate from within the corona or the HCS.

To better illustrate this region, Figure 5 shows a zoomed-in plot of the intermediate super-Alfvénic interval, identified as the region between two vertical lines in each panel. Alternating forward and backward slow modes (middle-bottom and right-bottom panels) coincide with large and small magnetic field magnitudes |B|, respectively. The abrupt drop of |B| at the edges is also associated with sharp changes in B_R , the radial proton velocity V_R , density n_p , and plasma beta. The outflow plasma jet is clearly shown in the radial direction (e.g., $\Delta V_R \sim 40 \text{ km s}^{-1}$ relative to the external flow). Although more rigorous evidence for an HCS reconnection exhaust needs further investigation, the alternating forward and backward

slow modes identified here could be signatures of a Petschektype reconnection configuration (e.g., Petschek 1964; Gosling et al. 2005), which are usually bounded by slow-shock-like structures embedded in an accelerated flow and have been observed prevalently in the near-Sun HCS by PSP (e.g., Phan et al. 2021).

3. Conclusions

After entering the sub-Alfvénic solar wind in 2021 April for the first time, the PSP sampled the sub-Alfvénic streams for an extended period during orbit 10, with the smallest Mach number being \sim 0.2. The turbulence properties and MHD waves during these periods have been analyzed in this paper. The main conclusions are listed as follows.

- 1. The sub-Alfvénic solar wind flows of E10 are observed to be Alfvénic and dominated by outward-propagating Alfvén waves (i.e., $\sigma_c \sim 1$ in the sunward magnetic field sector), which was also reported in the sub-Alfvénic solar wind observed in E8 and E9 (e.g., Kasper et al. 2021; Zhao et al. 2022b; Bandyopadhyay et al. 2022; Zank et al. 2022). The plasma speed within the observed sub-Alfvénic intervals was extremely low, with radial flow speed V_R less than 200 km s⁻¹, suggesting that the prevalent wind sampled by PSP was Alfvénic slow wind. Few switchbacks and a decrease in the anti-Sunward Strahl electron fluxes are observed in the two sub-Alfvénic intervals, where the low Mach number is mainly due to the slow solar wind speed and low plasma density. These features are consistent with switchbacks possibly generated on the boundaries of slow and fast wind regions by interchange reconnection at the Sun (Fisk & Kasper 2020; Zank et al. 2020). In the region between the two sub-Alfvénic flows, PSP observed possible partial HCS crossings, where the magnetic field magnitude |B|decreases to near zero but without direction changes in the radial magnetic field B_R . Low values of the normalized cross-helicity σ_c and highly negative normalized residual energy σ_r are observed near the partial HCS crossings, which are consistent with previous observations (Zhao et al. 2021c) and suggest the presence of convected solar wind structures with near-zero velocity fluctuations (e.g., Tu & Marsch 1991; Wang et al. 2020; Zhao et al. 2020).
- 2. While the turbulent power spectra for outward-propagating Elsässer z^+ mode steepens at high frequencies, the spectra for inward-propagating Elsässer z^- modes flatten. The flattening of the z^- spectrum is similar to that found in the Helios and PSP data (e.g., Tu et al. 1989; Zank et al. 2022). In this paper, the very low amplitude of the velocity fluctuation PSD at high frequencies suggests that the flattening of the z^- spectra may indeed be physical and possibly can be explained by the NI turbulence model. However, we cannot completely rule out the influence of noise. In the previous sub-Alfvénic flows observed by PSP in E8, the flow speed and mean magnetic field are quasi-aligned (i.e., $\theta_{\rm VB}^{\rm sc} \sim 0$) so that the 2D component is ignored in the NI model (Zank et al. 2022). However, during the two sub-Alfvénic flows observed in E10, θ_{VB}^{sc} deviates from parallel sampling. A complete modeling of the Elsässer spectra based on the NI MHD model needs to take into account the power of

- the 2D component. We find that the inclusion of the 2D component mainly affects the z^- power at low frequencies and can successfully reproduce the "concave" shape of the z^- spectra, and the z^+ spectra basically follow the -3/2 scaling in the inertial range and are mainly dominated by the NI/slab component.
- 3. MHD wave decomposition based on an isothermal assumption suggests that the two sub-Alfvénic intervals are dominated by outward-propagating Alfvén waves with a minority contribution from outward-propagating fast magnetosonic waves, which is consistent with our previous findings in the magnetic-field-aligned solar wind flows (Zhao et al. 2021a). In contrast, during the super-Alfvénic interval in between, slow magnetosonic modes with $\theta_{k,B_0} \sim 90^{\circ}$ clearly dominate. According to the MHD linear wave dispersion relation, the slow mode reduces to a nonpropagating pressure-balanced structure in the perpendicular wavevector limit, which has not been pointed out by previous studies using a similar methodology (Chaston et al. 2020; Zhu et al. 2020). Thus, the alternating forward and backward slow modes with perpendicular wavevectors identified here are in fact nonpropagating pressure-balanced structures and may also be features of Petschek-type reconnection near the HCS.

To summarize, our results are the first detailed analysis of waves and turbulence properties in the two robust sub-Alfvénic winds observed during PSP's 10th orbit. In this paper, we use a composite spectral model that includes both a counterpropagating Alfvénic component and a 2D component. The Alfvénic component is significantly Doppler shifted due to the low solar wind speed relative to the Alfvén speed while the 2D component is stationary and thus not Doppler shifted. This is the first time that a spectral model that includes both a Dopplershifted Alfvénic component and a stationary 2D component is used in solar wind data. In addition, the wave decomposition identifies Alfvén modes and fast magnetosonic modes during the two sub-Alfvénic flows. The example of the super-Alfvénic interval in between illustrates that the slow modes identified before by a similar method may be zero-frequency nonpropagating structures. Finally, modeling the solar wind turbulence in the sub-Alfvénic regime will be of interest to future studies.

We acknowledge the partial support of the NSF EPSCoR RII-Track-1 Cooperative Agreement OIA-1655280, NASA award 80NSSC20K1783, and NASA Parker Solar Probe contract SV4-84017. We thank S. Badman for fruitful discussions on the source of the solar wind observed by the Parker Solar Probe. We thank the NASA Parker Solar Probe SWEAP team led by J. Kasper and the FIELDS team led by S. D. Bale for use of data.

ORCID iDs

L.-L. Zhao https://orcid.org/0000-0002-4299-0490
G. P. Zank https://orcid.org/0000-0002-4642-6192
L. Adhikari https://orcid.org/0000-0003-1549-5256
D. Telloni https://orcid.org/0000-0002-6710-8142
M. Stevens https://orcid.org/0000-0002-7728-0085
J. C. Kasper https://orcid.org/0000-0002-7077-930X
S. D. Bale https://orcid.org/0000-0002-1989-3596
N. E. Raouafi https://orcid.org/0000-0003-2409-3742

References

```
Adhikari, L., Zank, G. P., Zhao, L. L., et al. 2020, ApJS, 246, 38
Andrés, N., Sahraoui, F., Hadid, L. Z., et al. 2021, ApJ, 919, 19
Badman, S. T., Bale, S. D., Martínez Oliveros, J. C., et al. 2020, ApJS, 246, 23
Bale, S., Badman, S., Bonnell, J., et al. 2019, Natur, 576, 237
Bale, S. D., Goetz, K., Harvey, P. R., et al. 2016, SSRv, 204, 49
Bale, S. D., Horbury, T. S., Velli, M., et al. 2021, ApJ, 923, 174
Bandyopadhyay, R., Goldstein, M. L., Maruca, B. A., et al. 2020, ApJS,
   246, 48
Bandyopadhyay, R., Matthaeus, W. H., McComas, D. J., et al. 2022, ApJL,
  926, L1
Bandyopadhyay, R., & McComas, D. J. 2021, ApJ, 923, 193
Belcher, J., & Davis, L., Jr 1971, JGR, 76, 3534
Chaston, C., Bonnell, J., Bale, S., et al. 2020, ApJS, 246, 71
Chen, C., Bale, S., Bonnell, J., et al. 2020, ApJS, 246, 53
Drake, J. F., Agapitov, O., Swisdak, M., et al. 2021, A&A, 650, A2
Fisk, L. A., & Kasper, J. C. 2020, ApJL, 894, L4
Fox, N., Velli, M., Bale, S., et al. 2016, SSRv, 204, 7
Glassmeier, K., Motschmann, U., & Stein, R. 1995, AnGeo, 13, 76
Goldstein, M. L., Roberts, D. A., & Matthaeus, W. H. 1986, JGR, 91, 13357
Gosling, J. T., Skoug, R. M., McComas, D. J., & Smith, C. W. 2005, JGRA,
   110, A01107
Horbury, T. S., Forman, M., & Oughton, S. 2008, PhRvL, 101, 175005
Kasper, J. C., Abiad, R., Austin, G., et al. 2016, SSRv, 204, 131
Kasper, J. C., Bale, S. D., Belcher, J. W., et al. 2019, Natur, 576, 228
```

Kasper, J. C., Klein, K. G., Lichko, E., et al. 2021, PhRvL, 127, 255101

```
Matthaeus, W. H., Zank, G. P., Oughton, S., Mullan, D., & Dmitruk, P. 1999,
   ApJL, 523, L93
Moncuquet, M., Meyer-Vernet, N., Issautier, K., et al. 2020, ApJS, 246, 44
Petschek, H. E. 1964, in Proc. of the AAS-NASA Symp., The Physics of Solar
   Flares, ed. W. M. Hess (Washington, DC: National Aeronautics and Space
   Administration), 425
Phan, T. D., Lavraud, B., Halekas, J. S., et al. 2021, A&A, 650, A13
Santolík, O., Parrot, M., & Lefeuvre, F. 2003, RaSc, 38, 1010
Telloni, D., Sorriso-Valvo, L., Woodham, L. D., et al. 2021, ApJL, 912, L21
Tu, C. Y., & Marsch, E. 1991, AnGeo, 9, 319
Tu, C. Y., Marsch, E., & Thieme, K. M. 1989, JGR, 94, 11739
Wang, X., Tu, C., & He, J. 2020, ApJ, 903, 72
Whittlesey, P. L., Larson, D. E., Kasper, J. C., et al. 2020, ApJS, 246, 74
Zank, G., Adhikari, L., Hunana, P., et al. 2017, ApJ, 835, 147
Zank, G., Adhikari, L., Hunana, P., et al. 2018, ApJ, 854, 32
Zank, G., Nakanotani, M., Zhao, L.-L., Adhikari, L., & Telloni, D. 2020, ApJ,
  900, 115
Zank, G. P., Nakanotani, M., Zhao, L. L., Adhikari, L., & Kasper, J. 2020, ApJ,
   903, 1
Zank, G. P., Zhao, L. L., Adhikari, L., et al. 2021, PhPl, 28, 080501
Zank, G. P., Zhao, L. L., Adhikari, L., et al. 2022, ApJL, 926, L16
Zhao, L. L., Zank, G. P., Adhikari, L., et al. 2020, ApJS, 246, 26
Zhao, L. L., Zank, G. P., Adhikari, L., & Nakanotani, M. 2022a, ApJL, 924, L5
Zhao, L. L., Zank, G. P., He, J. S., et al. 2021a, ApJ, 922, 188
Zhao, L. L., Zank, G. P., He, J. S., et al. 2021b, A&A, 656, A3
Zhao, L. L., Zank, G. P., Hu, Q., et al. 2021c, A&A, 650, A12
Zhao, L. L., Zank, G. P., Telloni, D., et al. 2022b, ApJL, 928, L15
Zhu, X., He, J., Verscharen, D., Duan, D., & Bale, S. D. 2020, ApJL, 901, L3
```